Electron-Beam Powder Bed Fusion of High-Carbon Co-Cr-Mo Alloys for Industrial Applications

Kenta Yamanaka, Shoya Aota, Manami Mori, Nobuyuki Sasaki, Jerome Adrien, Eric Maire, Damien Fabregue, Akihiko Chiba

J. Jpn. Soc. Powder Powder Metallurgy, **72** (2025) S409-S414
https://doi.org/10.2497/jjspm.15B-T6-08

Electron-Beam Powder Bed Fusion of High-Carbon Co–Cr–Mo Alloys for Industrial Applications

Kenta YAMANAKA[1]*, Shoya AOTA[1], Manami MORI[2], Nobuyuki SASAKI[1], Jerome ADRIEN[3], Eric MAIRE[3], Damien FABREGUE[3], and Akihiko CHIBA[1]

[1]Tohoku University, 2-1-1 Katahira, Aoba-ku, Sendai 980-8577, Japan.
[2]National Institute of Technology, Sendai College, 48 Nodayama, Medeshima-Shiote, Natori 981-1239, Japan.
[3]INSA-Lyon, 20 Avenue Einstein, 69621 Villeurbanne, France.

Abstract

In this study, through electron-beam powder bed fusion additive manufacturing, we prepared Co–27Cr–6Mo (wt.%) alloys with different C concentrations up to the eutectic composition (~2.5 wt.%). The Rockwell hardness of the as-built alloy specimens increased linearly with an increase in the carbon concentration, reaching approximately 60 HRC at 2.5 wt.% C. The as-built 2.5C alloy contained a fine carbide network consisting of M_7C_3- and $M_{23}C_6$-type carbide phases. Increasing the carbon concentration not only increased the carbide fraction and changed the carbide phases but also altered the solidification behavior from cellular at low carbon concentrations to dendritic and finally to eutectic. Quantitative X-ray tomography revealed that carbon addition also affected the gas pore behavior in the melt pool, significantly reducing the porosity when a flat solid/liquid front existed upon solidification (i.e., planar and eutectic). The developed high-carbon alloys cannot be obtained through conventional metal processing; hence, this study opens new avenues for industrial applications of additive manufacturing.

Keywords: additive manufacturing, electron-beam powder bed fusion, Co–Cr–Mo alloys, hardness, gas pores

Introduction

Owing to their excellent corrosion resistance, wear resistance, and biocompatibility, Co–Cr–Mo alloys have been used in orthopedic applications such as total hip arthroplasty, knee prostheses, spinal instrumentation surgery, and dental restorations[1–5]. The strengthening mechanisms of biomedical Co–Cr–Mo alloys have been explored. Thermomechanical processing is the primary approach; significant grain refinement and dislocation strengthening due to low stacking fault energies at elevated temperatures have been reported[6–14]. Carbide precipitation is frequently employed in biomedical Co–Cr–Mo alloys. According to the ASTM F75 standard, carbon concentrations of up to 0.35 wt.% are allowed for biomedical-grade alloys. Further carbon addition, which leads to massive carbide precipitation, is challenging in conventional manufacturing processes, such as hot rolling, forging, and swaging, as the alloy becomes prone to cracking.

Additive manufacturing (AM) is attracting increasing attention as an innovative manufacturing technology because it allows the fabrication of complex geometries and tailoring of the microstructures and resulting mechanical properties of metallic materials[15–20]. Biomedical Co–Cr–Mo alloys have been extensively explored using electron-beam[21–25] and laser[26–32] powder bed fusion technologies (EB-PBF and L-PBF, respectively). The PBF Co–Cr–Mo alloys generally consist of columnar microstructures of the face-centered cubic (FCC) γ-phase where the <001> direction is aligned with the building direction[24–26,33]. The precipitation of $M_{23}C_6$-type carbides was also observed at the columnar grain boundaries of the as-built alloys[21]. Tan et al.[22] reported the formation of two types of carbides, i.e., $M_{23}C_6$ and M_6C, in EB-PBF Co–28.5Cr–6Mo–0.22C–0.15N alloys. It has been demonstrated that EB-BPF allows the homogeneous distribution of fine carbide precipitates in these alloys, which cannot be attained via casting. Moreover, AM can handle difficult-to-process materials that contain large amounts of precipitates[34].

In this study, we prepared high-carbon Co–Cr–Mo alloys with carbon concentrations up to 2.5 wt.%[35] and explored the microstructures and mechanical properties of the as-built specimens prepared via EB-PBF. Moreover, using X-ray computed tomography (XCT), the gas pores in the as-built specimens, which significantly affect their mechanical properties[36,37], were quantitatively evaluated and compared with those in the raw powders.

Experiment

Five Co–27Cr–6Mo–*x*C (wt.%) alloy powders with different carbon contents (ranging from 0.04 to 2.5 wt.%) were prepared in this study. Table 1 presents the chemical compositions of the prepared powders. Hereinafter, these alloys are denoted as the 0.04C, 0.22C, 1.5C, 2.0C, and 2.5C alloys. The 0.04C and 0.22C alloy powders satisfied the ASTM F75 standard for biomedical Co–Cr–Mo alloys. 0.22C powder was purchased from AP&C (Canada), and Ar gas atomization was used to produce the other powders at Sanyo Special Steel (Japan). The prepared powders had similar particle-size distributions, but the gas-atomized powders exhibited a satellite peak at approximately 20 μm. The average diameters (d_{50}) for the powders are shown in Table 1.

Table 1 Chemical compositions (wt.%) and average diameters (d_{50}, μm) of the raw powders.

Alloy	Co	Cr	Mo	Ni	Si	Mn	Fe	N	C	d_{50}
0.04C	Bal.	27.0	5.86	<0.05	0.40	0.53	0.09	0.11	0.03	50.2
0.22C	Bal.	27.1	5.60	<0.05	0.25	0.55	0.32	0.13	0.21	52.4
1.5C	Bal.	26.6	5.85	<0.05	0.41	0.55	0.12	0.04	1.40	47.0
2.0C	Bal.	26.1	5.87	<0.05	0.38	0.53	0.10	0.03	1.91	50.2
2.5C	Bal.	26.3	5.95	<0.05	0.41	0.54	0.15	0.02	2.47	48.6

*corresponding author, E-mail: kenta.yamanaka.c5@tohoku.ac.jp

Thin-wall specimens 20 mm wide, 2 mm thick, and 20 mm high, were manufactured using an Arcam A2X system (Sweden). Supports with a height of 5 mm were developed at the bottom of the thin walls during the fabrication. Identical building conditions (Table 2), which were based on the manufacturer's standard conditions for Co–Cr–Mo alloys, were employed for each powder so that we could examine the carbon concentration dependence.

Table 2 Building parameters.

Parameters	Value
Preheating temperature (°C)	850
Beam current (mA)	5.5
Speed function (–)	25
Focus offset (mA)	15
Line offset (mm)	0.2
Layer thickness (μm)	70

The as-built microstructures of the specimens were examined using scanning electron microscopy (SEM, S-3400, JEOL) at 15 kV. Additionally, electron backscatter diffraction analysis was conducted using a field-emission scanning electron microscope (FESEM, XL30S-FEG, FEI, USA) operated at 20 kV with the OIM Data Collection/Analysis software (ver. 7.3, EDAX, USA). Elemental mapping of the as-built specimens was performed using field-emission electron probe microanalysis (EPMA, JXA-8530F, JEOL, Japan) at 15 kV. The Rockwell hardness (HRC) of the as-built specimens were measured using a DXT-10 instrument (Matsuzawa, Japan). The samples for the aforementioned microstructural/mechanical characterizations were prepared via a conventional metallographic procedure with emery paper and polishing with a 0.3-μm Al_2O_3 suspension (AP-A, Struers, Japan) and a 0.04-μm colloidal SiO_2 solution (OP-U, Struers, Japan). Scanning transmission electron microscopy (STEM) and energy-dispersive X-ray spectroscopy (EDS) elemental mapping were performed on the as-built 2.5C alloy specimen using a double spherical aberration-corrected STEM instrument (Titan^3 G2 60-300, FEI, USA) equipped with a Super-X EDS detector operated at an accelerating voltage of 300 kV. The sample for STEM-EDS analysis was prepared using a focused ion beam (Helios NanoLab 600i dual-beam, FEI, USA). Thermodynamic calculations were performed using the Thermo-Calc software (ver. 2022a; TCNI8: Ni-Alloys v8.6; Thermo-Calc Software, Sweden).

The XCT measurements of the raw powders and as-built specimens were performed using a Phoenix V|tome|X system (GE, USA)[38] with an accelerating voltage of 100 kV. Each powder was encapsulated in a polymer tube during the XCT measurements. Voxel sizes of 2.0 and 1.5 μm were employed for evaluating the gauge portions of the powders and as-built specimens, respectively. The gas pores in the powders and as-built specimens were analyzed using 3D ImageJ Suite,[39] and 3D reconstruction and quantitative evaluation of the pores were performed using Fiji ImageJ[40]. The analytical procedures are described in Ref.[35].

Results and Discussion

Fig. 1 illustrates the relationship between the carbon concentration and Rockwell hardness of the as-built specimens[35]. There was a linear correlation between the hardness and carbon concentration in the investigated range. The as-built 2.5C alloy specimen exhibited a high Rockwell hardness of approximately 60 HRC, which is comparable to those of high-carbon martensitic stainless steels (e.g., SUS440C).

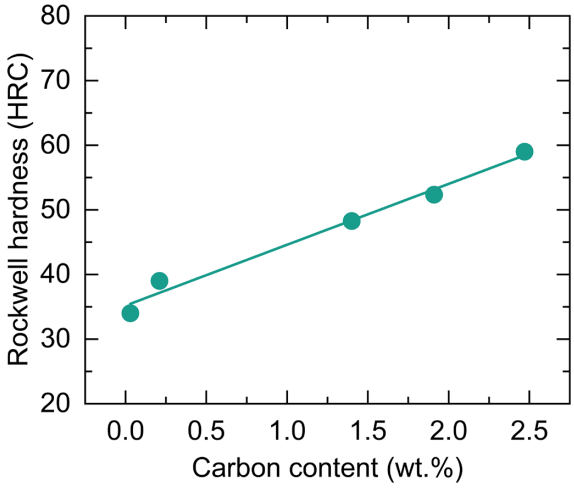

Fig. 1 Rockwell hardness of the as-built alloy specimens as a function of the carbon concentration[35].

Fig. 2 shows SEM backscattered electron (BSE) images of the as-built specimens. The 0.04C and 0.22C alloy specimens (Figs. 2(a) and (b)) exhibited columnar microstructures with precipitates at the grain boundaries. The 1.5C and 2.0C alloy specimens (Figs. 2(c) and (d)) exhibited well-defined dendritic microstructures with two types of precipitates of different contrasts in the SEM-BSE images. The 2.5C alloy specimen featured a solidification microstructure consisting of numerous precipitates, although its morphology differed from those of the 1.5C and 2.0C alloys.

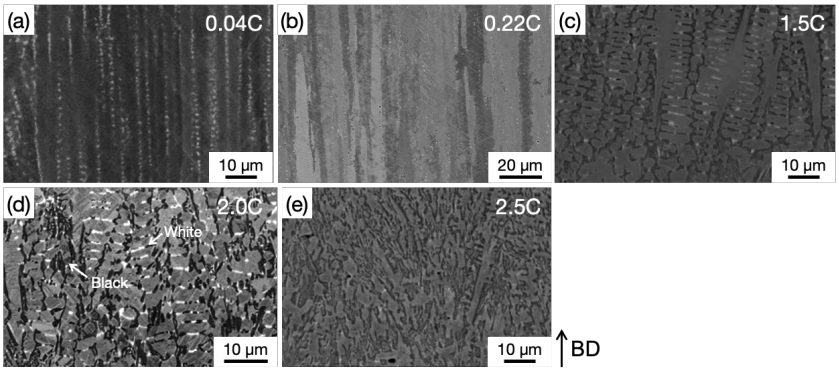

Fig. 2 Cross-sectional SEM-BSE images of the as-built alloy specimens: (a) 0.04C, (b) 0.22C, (c) 1.5C, (e) 2.0C, and (d) 2.5C.

Fig. 3 shows the SEM-BSE images and EPMA elemental maps of the as-built specimens[35]. The grain-boundary precipitates in the as-built 0.04C alloy specimen were enriched with Cr, Mo, and Si (Fig. 3(a)). Although the 0.22C alloy specimen exhibited a similar elemental distribution, as shown in Fig. 3(b), the precipitated phase changed to the carbide phase(s)[22]. The as-built 1.5C, 2.0C, and 2.5C alloy specimens (Figs. 3(c)–(f)) had more complex solidification microstructures consisting of carbide precipitate networks enriched with Cr, Mo, and C. Two different carbide phases were observed in each image, with Si preferentially partitioning into the white phase and the black phase containing a higher carbon concentration than the white particles.

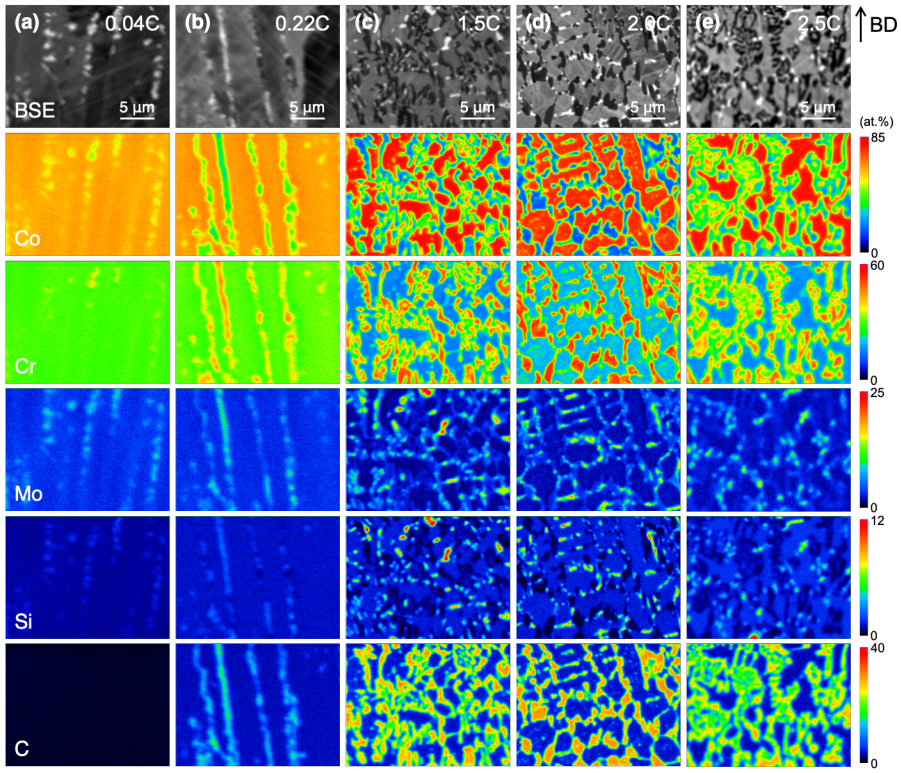

Fig. 3 Cross-sectional SEM-BSE images and corresponding EPMA elemental maps of the as-built specimens: (a) 0.04C, (b) 0.22C, (c) 1.5C, (e) 2.0C, and (d) 2.5C alloys[35].

Fig. 4 shows the STEM-EDS results for the as-built 2.5C alloy specimen, revealing an ultrafine-grained multiphase microstructure in the annular bright-field (ABF) and high-angle annular dark-field (HAADF) STEM images (Figs. 4(a) and (b)). The elemental maps indicated three distinct phases with different compositions, as shown in Fig. 4(b). The Co-rich area (Area #1) corresponds to the γ-phase; planar dislocation substructures are observed in the grain interior. In contrast, both the Cr-rich (Area #2) and Mo-rich (Area #3) areas are attributed to the formation of different carbide phases. Table 3 presents the quantitative chemical composition of each area. According to thermodynamic calculations, the Cr- and Mo-rich carbides were determined to be M_7C_3 and $M_{23}C_6$, respectively. Boron, which may be an impurity, was also detected in the Mo-rich carbide. The high hardness of the 2.5C alloy specimen is attributed to massive carbide precipitation.

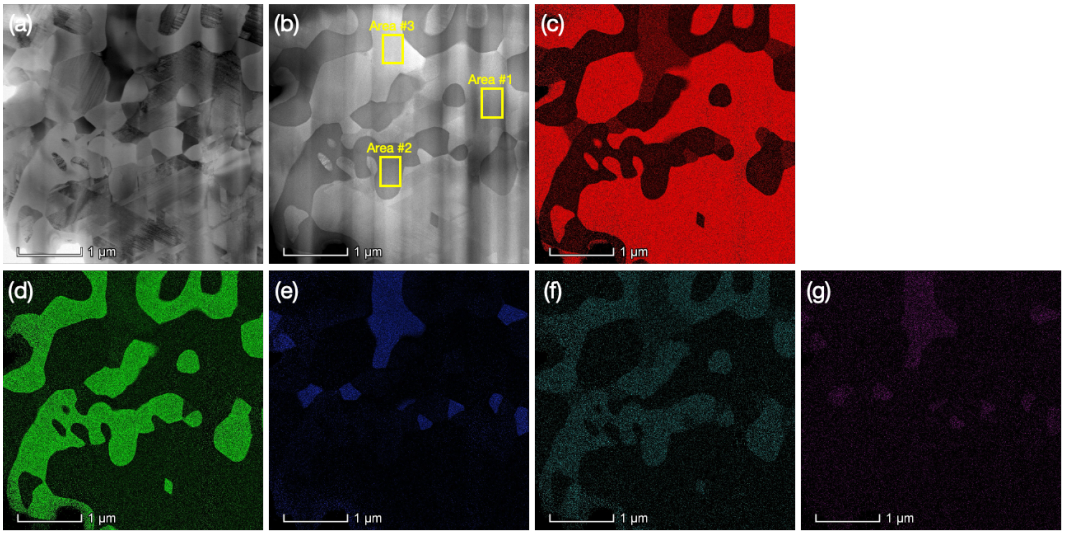

Fig. 4 STEM-EDS analysis results for the as-built 2.5C alloy specimen: (a) ABF-STEM and (b) HAADF-STEM images; elemental maps of (c) Co, (d) Cr, (e) Mo, (f) C, and (g) B.

Table 3 Chemical compositions of the three areas indicated in Fig. 4(b) (at.%).

Area	Co	Cr	Mo	C	B
#1	80.0	11.1	1.4	6.0	1.5
#2	16.5	50.1	3.6	24.7	5.1
#3	30.7	13.8	22.1	9.3	24.1

The transition in the carbide phase aligned with the calculated phase diagram (Fig. 5(a)). Increasing the carbon concentration stabilized the γ (FCC)-phase directly solidified from the liquid phase, with precipitated phase transitioning from intermetallic compounds (σ) to $M_{23}C_6$-type carbides and finally to M_7C_3-type carbide at higher carbon contents. The 2.5C alloy had a near-eutectic composition. The difference in the solidification behavior resulted in a different carbide morphology with a slightly lower carbon concentration in the carbides compared with the 2.0C alloy. Therefore, the solidification behavior of Co–Cr–Mo alloys varies from planar (0.04C and 0.22C) to dendritic (1.5C and 2.0C) and finally to eutectic microstructure at 2.5 wt.% carbon. Fig. 5(b) shows that the γ- and M_7C_3 carbide phases are produced from the liquid phase upon eutectic solidification. Moreover, the $M_{23}C_6$-type carbide, which was also observed in the as-built 2.5C alloy specimen, should appear during cooling after fabrication via a solid-state phase transformation.

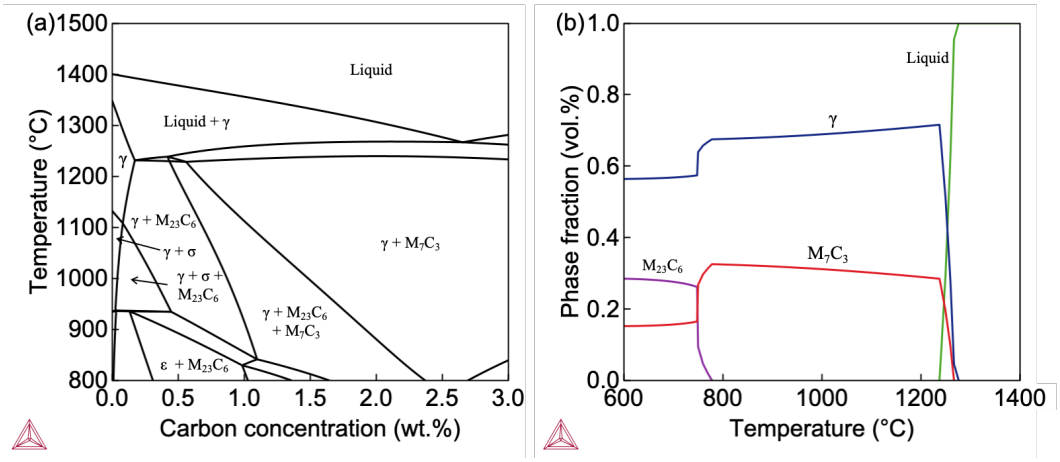

Fig. 5 Results of thermodynamic calculations: (a) vertical section of the phase diagram for the Co–27Cr–6Mo–*x*C (wt.%) system and (b) phase fractions for the Co–27Cr–6Mo–2.5C (wt.%, 2.5C) alloy with respect to the temperature.

Fig. 6 shows the relationship between the carbon concentration and porosity (measured using tomography images) of the raw powders and their as-built specimens[35]. The porosity (i.e., the gas pores entrapped during atomization) of the raw powders increased with an increase in the carbon concentration because of the reduced liquidus temperature, allowing a longer liquid state during the atomization process at higher carbon contents (Fig. 5(a)). However, the as-built alloy specimens were generally almost fully dense, with porosity values of <0.2 vol.% for all carbon concentrations. This indicated that gas bubbles originating from the raw powders were eliminated from the melt pool during the EB-PBF process. Both the as-built 0.04C and 0.22C alloy specimens exhibited negligible gas pores. The porosity of the as-built alloy specimens exhibited a non-monotonous carbon-concentration dependence, with a maximum value of ~0.15 vol.% for the 2.0C alloy. Notably, the as-built 2.5C alloy exhibited remarkable pore elimination upon solidification during EB-PBF. The 2.5C alloy near the eutectic composition should have a flat/smooth migrating solid/liquid interface, similar to that in planar solidification at lower carbon contents (i.e., 0.04C and 0.22C alloys). Therefore, the significant reduction in porosity at the

eutectic composition is attributed to transitions in the solidification behavior.

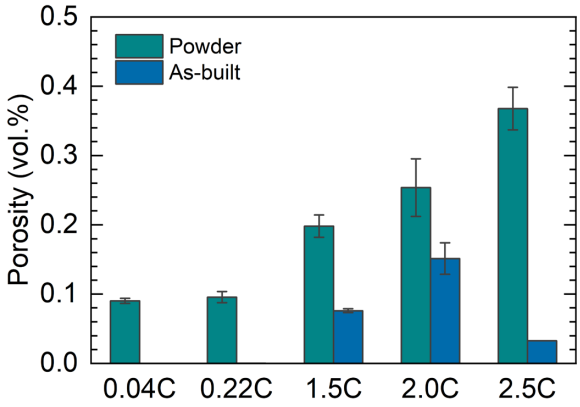

Fig. 6 Volume fractions of gas pores in the raw powders and as-built specimens with respect to the carbon concentration[35].

Conclusion

In this study, five different Co–Cr–Mo–C alloy powders and their consolidated specimens were prepared using EB-PBF. The findings are summarized as follows:

- The Rockwell hardness of the as-built specimens increased with the carbon concentration, reaching a remarkably high value of approximately 60 HRC for the 2.5C alloy.
- The as-built 2.5C alloy specimen exhibited an ultrafine multiphase microstructure consisting of M_7C_3- and $M_{23}C_6$-type carbide phases. The formation of carbide phases, which was promoted by the addition of carbon, was responsible for the enhanced hardness. Thermodynamic calculations suggested that M_7C_3 carbide was formed upon solidification, whereas $M_{23}C_6$-type carbide was formed via a solid-state phase transformation during cooling.
- The porosity of the raw powders increased with the carbon content. This is attributed to the reduction in the liquidus temperature as the carbon content increased.
- The EB-PBF process eliminated the powder-originated gas pores, resulting in nearly full densification in the 0.04C and 0.22C alloys. While the as-built 1.5C and 2.0C alloys, which underwent dendritic solidification, exhibited reduced pore elimination, further increasing the carbon concentration to the eutectic composition (2.5 wt.%) significantly reduced the porosity of the solidified samples.

Acknowledgement

The authors thank Issei Narita, Yukiko Kodama, and Yuichiro Hayasaka for their technical assistance. EPMA was performed at the Cooperative Research and Development Center for Advanced Materials, Institute for Materials Research, Tohoku University [proposal number 18G0417]. This research was conducted under the ELyT Global Program and financially supported from the Japan Society for the Promotion of Science (JSPS) [grant numbers 18H03834, 18H05455, and 23K26415].

References

1) A. Chiba, K. Kumagai, N. Nomura, S. Miyakawa: Acta Mater., **55** (2007) 1309–1318.
2) S. Mischler, A.I. Muñoz: Wear, **297** (2013) 1081–1094.
3) Y. Chen, Y. Li, S. Kurosu, K. Yamanaka, N. Tang, Y. Koizumi, A. Chiba: Wear, **310** (2013) 51–62.
4) Y. Koizumi et al.: Acta Mater., **61** (2013) 1648–1661.
5) H.S. Dobbs, J.L.M. Robertson: J. Mater. Sci., **18** (1983) 391–401.
6) A.J. Saldívar-García, H.F. López: J. Biomed. Mater. Res. A, **74A** (2005) 269–274.
7) O. Öztürk, U. Türkan, A.E. Eroğlu: Surf. Coat. Technol., **200** (2006) 5687–5697.
8) K. Yamanaka, M. Mori, A. Chiba: Metall. Mater. Trans. A, **43** (2012) 5243–5257.
9) M. Mori et al.: Acta Biomater., **28** (2015) 215–224.
10) F. Ren, W. Zhu, K. Chu: J. Mech. Behav. Biomed. Mater., **60** (2016) 139–147.
11) K. Yamanaka, M. Mori, S. Sato, A. Chiba: Sci. Rep., **7** (2017) 10808.
12) E. Zhang, Y. Ge, G. Qin: J. Mater. Sci. Technol., **34** (2018) 523–533.
13) K. Yamanaka, M. Mori, I. Kartika, M.S. Anwar, K. Kuramoto, S. Sato, A. Chiba: Corros. Sci., **148** (2019) 178–187.
14) N. Gong et al.: J. Biomed. Mater. Res. B Appl. Biomater., **108** (2020) 1518–1526.
15) T. DebRoy et al.: Prog. Mater. Sci., **92** (2018) 112–224.
16) D. Herzog, V. Seyda, E. Wycisk, C. Emmelmann: Acta Mater., **117** (2016) 371–392.

17) W.J. Sames, F.A. List, S. Pannala, R.R. Dehoff, S.S. Babu: Int. Mater. Rev., **61** (2016) 315–360.
18) J.H. Martin, B.D. Yahata, J.M. Hundley, J.A. Mayer, T.A. Schaedler, T.M. Pollock: Nature, **549** (2017) 365–369.
19) J.J. Lewandowski, M. Seifi: Annu. Rev. Mater. Res., **46** (2016) 151–186.
20) Y.M. Wang et al.: Nat. Mater., **17** (2018) 63–70.
21) S.H. Sun, Y. Koizumi, S. Kurosu, Y.P. Li, H. Matsumoto, A. Chiba: Acta Mater., **64** (2014) 154–168.
22) X.P. Tan et al.: Scr. Mater., **143** (2018) 117–121.
23) Y. Zhao, Y. Koizumi, K. Aoyagi, D. Wei, K. Yamanaka, A. Chiba: Addit. Manuf., **26** (2019) 202–214.
24) Y. Zhao, Y. Koizumi, K. Aoyagi, D. Wei, K. Yamanaka, A. Chiba: Materialia, **6** (2019) 100346.
25) D.D. Xiang et al.: Mater. Sci. Eng. A, **765** (2019) 138270.
26) A. Takaichi et al.: J. Mech. Behav. Biomed. Mater., **21** (2013) 67–76.
27) G. Barucca et al.: Mater. Sci. Eng. C, **48** (2015) 263–269.
28) B. Qian, K. Saeidi, L. Kvetková, F. Lofaj, C. Xiao, Z. Shen: Dent. Mater., **31** (2015) 1435–1444.
29) X. Zhou, D. Wang, X. Liu, D.D. Zhang, S. Qu, J. Ma, G. London, Z. Shen, W. Liu: Acta Mater., **98** (2015) 1–16.
30) E. Liverani, A. Fortunato, A. Leardini, C. Belvedere, S. Siegler, L. Ceschini, A. Ascari: Mater. Des., **106** (2016) 60–68.
31) S.L. Sing, S. Huang, W.Y. Yeong: Mater. Sci. Eng. A, **769** (2020) 138511.
32) Z. Wang et al.: Addit. Manuf., **37** (2021) 101725.
33) L.E. Murr: Addit. Manuf., **5** (2015) 40–53.
34) H. Shiratori, T. Fujieda, K. Yamanaka, Y. Koizumi, K. Kuwabara, T. Kato, A. Chiba: Mater. Sci. Eng. A, **656** (2016) 39–46.
35) S. Aota, K. Yamanaka, M. Mori, N. Sasaki, J. Adrien, E. Maire, D. Fabrègue, A. Chiba: Addit. Manuf., **59** (2022) 103134.
36) X. Shui, K. Yamanaka, M. Mori, Y. Nagata, K. Kurita, A. Chiba: Mater. Sci. Eng. A, **680** (2017) 239–248.
37) R. Cunningham et al.: Mater. Res. Lett., **5** (2017) 516–525.
38) J.Y. Buffiere, E. Maire, J. Adrien, J.P. Masse, E. Boller: Exp. Mech., **50** (2010) 289–305.
39) J. Ollion, J. Cochennec, F. Loll, C. Escudé, T. Boudier; Bioinformatics, **29** (2013) 1840–1841.
40) J. Schindelin et al.: Nat. Methods, **9** (2012) 676–682.

Received July 26, 2024; Revised October 17, 2024; Accepted October 22, 2024